ITN-5VC

Integrated Telematics for Next Generation 5G Vehicular Communications

ITN-5VC D1.1

Report on phased array MIMO antenna numerical models

Version v1.0 Date: 2022/11/30

Document properties:

Grant Number:	955629
Document Number:	D1.1
Document Title:	Report on phased array MIMO antenna numerical models
Partners involved:	University of Twente, Gapwaves
Authors:	Reza Gheybi Zarnagh, Coen van de Ven, and Andrés Alayón Glazunov (Editor)
Contractual Date of Delivery:	2022/11/30
Dissemination level:	PU[1]
Version:	1.0
File Name:	ITN-5VC D1.1_v1.0

[1] CO = Confidential, only members of the consortium (including the Commission Services)

PU = Public

Table of Contents

Executive summary

This deliverable presents a report on phased array MIMO antenna numerical models and simulations. The objectives of these simulations are to obtain optimized electromagnetic models of multi-purpose phased arrays at mm-Wave frequency bands for automotive applications and optimized electromagnetic models of RADAR phased array antenna at mm-Wave frequency bands. The deliverable is a collaboration of ESR 1 and ESR 3 involved in WP1 and they are working on the producing numerical models and design and fabrication of phased array antennas for Joint Communication/Sensing (JC&S) and automotive radar applications. The numerical of the antennas have been produced by the CST Microwave Studio simulation software. Some of the presented results have summarized in papers [A] and [B] and have been submitted to the EuCAP 2023 conference.

[A] R. Gheybi Zarnagh, A. A. Glazunov, “Correlation and Non-Orthogonality Figures of Merit of Beamforming Fields,” EuCAP2023.

[B] C. van de Ven A. A. Glazunov, “Automotive RADAR Planar Antenna Optimization Based on Conformal Transformation Optics,” EuCAP2023.

List of figures

List of tables

List of acronyms and abbreviations

2D	Two dimensional
3D	Three dimensional
CTO	Conformal Transformation Optics
EBG	Electromagnetic Band Gap
ESR	Early-Stage Researcher
FoV	Field of view
IC	Integrated Circuit
JC&S	Joint communication and censing
MIMO	Multiple-Input Multiple-Output
mm-Wave	millimetre wave
OTA	Over The Air
PCB	Printed circuit board
TEM	Transverse Electro-Magnetic
V2X	Vehicular-to-ever
WP1	Work Package 1
UT	University of Twente

1 Introduction

Work Package 1 (WP1) of the ITN-5VC project focus on the design of mm-Wave phased array MIMO antennas for 5G V2X communications and sensing as well as on developing cost effective over the air (OTA) characterization methods of said antennas. Figures of merits reflecting system performance of the phased array MIMO antennas at mm-Waves are defined too. The latter focus on the spatial throughput coverage of the antennas. Moreover, guidelines on the deployment and OTA characterization of mm-Waves MIMO antennas mounted on cars are to be produced for both communications and sensing and provide channel models specific of mm-Waves 5G V2X communications for the system characterization.

WP1 are mainly contributed by ESR 1, ESR 2, ESR 3, ESR 4 and ESR 7. The Deliverable 1.1 presented here shows the numerical models which have been produced by ESR 1 and ESR 3.

In this report, we present various aspects related to WP1 addressing the following points.

- Antenna topologies for mm-Wave phased arrays
- Modelling techniques for RADAR phased array antennas at mm-Wave
- Modelling techniques for multipurpose phased array antennas at mm-Wave

2 Antenna topologies for mm-Wave phased arrays

2.1 PCB technology

At mm-Wave, losses become a major issue in the design of antennas. Also, the small wavelength requires high integration of the array with the active electronics which pose challenges due to miniaturization. A variety of antenna-types can be designed based on the PCB technology allowing to connect the ICs on the same board. The most common type of PCB antenna is the patch antenna and is still widely used in phased array applications at mm-Wave.

Patch antennas are based on an open resonant, typically rectangular, structure on the PCB. When this structure is properly impedance matched and fed with its resonant frequency, a resonant mode is excited which radiates a linear polarized wave. Combining multiple patches, the radiation pattern can be shaped.

2.2 Gap waveguide technology

Although PCB technology has proven its feasibility at mm-Wave, the dielectric losses in this technology are very much unwanted. Depending on the exact structure and the material properties, PCB based microstrip lines have been found to have a loss in the order of 0.8 dB/cm. For Gap waveguide (GW) technology, a similar section of routing has loss of <0.2 dB/cm. This reduction in loss is very beneficial especially for larger phased arrays because it directly improves the link budget by overcoming high path loss at the mm-Waves.

A typical antenna made with the GW technology is the slotted waveguide antenna. In the series fed patch array, the radiating pattern can be shaped by changing the number of elements and controlling the excitation of these elements. Besides this, additional structures can be added next to the slotted waveguide to help in shaping the radiation pattern.

The slotted waveguide antenna allows for a very narrow element in the horizontal dimension because vertically oriented slots radiate horizontal-polarized waves . Hence, GW antennas can be designed with a wide Field of View (FoV).

In addition to the advantages of GW antennas in terms of electrical performance, the mechanical stack up of this type of antenna does not need a galvanic contact. This means that it is possible to have a small gap between each layer, which greatly reduces the sensitivity to manufacturing tolerance compared to other waveguide-based solutions. Therefore, GW antennas can be produced at large scale at low cost.

3 Modelling techniques for RADAR phased array antennas at mm-Wave

3.1 Full-wave simulation

Designing phased array antennas, e.g., for RADAR applications, requires to evaluate the geometry in an electromagnetic simulator. This is because due to the complexity of the antennas, analytical models do not exist, and thus numerical techniques are used. Also, the typical size of RADAR antennas is in the order of 1-5 wavelengths with features going below 0.1 wavelength, which require full wave simulations performed by means of an electromagnetic simulator. The CST Studio Suite has been used to obtain many of the full wave simulations results presented in this report. The availability of the time and frequency domain solvers in the CST allows for accurate calculation of the electrical characteristics of the design. Also, the eigenmode solver can be used to the design of EBG structures as well as resonant structures.

The electrical requirements for the phased array antennas at mm-Wave for RADAR are mainly governed by the link budget within a certain FoV as well as the required accuracy and resolution. Typically, the required antenna gain is found from the link budget. The FoV of the antenna is defined by the link budget at the edges of the FoV of the RADAR system. The array layout is then found from the required angular resolution. Isolation between channels as well as pattern consistency mainly play a role for RADAR with a wide FoV and is typically constraint by the necessary accuracy and resolution.

3.2 Research gap with radome integration

The design flexibility of the slotted waveguide offers a control of the radiating pattern of these type of antennas. However, there are still a few limitations when it comes to the full design of the phased array. One feature responsible for several limitations is the addition of a radome to the antenna. The radome is the cover of the RADAR which acts as protection for the system. Typically, the antenna radome is a flat slab of plastic, half a wavelength in thickness. This thickness minimizes the negative effect of the radome for broadside radiation and reception.

For RADAR systems with a wider FoV, the half-wave thickness of the radome is inadequate to maintain the required radiation pattern. This is due to the impedance mismatch between free space and the radome. This mismatch results in reflections at the inside surface of the radome, exciting traveling waves between the antenna surface and in the radome. Moreover, the thickness of the radome cannot be reduced to eliminate propagating modes inside the radome. These modes might be excited and radiate from edges and discontinuities of the radome, which further deteriorates the radiation pattern.

A few solutions have been proposed to mitigate these problems using frequency selective surfaces, absorbers or EBGs. ESR3 work aims to not only mitigate the abovementioned limitations, but also use the dielectric constant inside the radome to enhance the radiation pattern in terms of beamwidth and ripples in the main beam. Transformation optics allows us to shape the radiation pattern. The Conformal Transformation Optics (CTO) technique can be implemented using varying dielectric constants.

4. Conformal Transformation Optics modelling techniques

Conformal transformation optics (CTO) is based on the implementation of conformal coordinate transformations by changing the dielectric constants in the spatial domain of interest. A few different approaches exist to compute this coordinate transformation, such as the Schwarz-Christoffel mapping or using the Laplace equation. Although the Schwarz-Christoffel mapping has a closed form solution, it is typically computed numerically.

Laplace equation is especially convenient to solve for quadrilateral geometries because a duality exists between the conformal transformation and the computation of a Transverse Electro-Magnetic (TEM) mode inside a Quadrilateral. This duality can be exploited to jointly optimize the CTO and the antenna element. ESR 3 has successfully used this duality to minimize the ripple on the radiation pattern of a slot antenna. This will be discussed in more detail in section 4.2.

4.1 Dielectric implementation and optical path rescaling

The mayor benefit of the CTO approach is that it can be implemented via the refractive index

$$n(x,y) = |\nabla W(x,y)|, \quad (1)$$

where $W(x,y)$ is the 2D-coordinate transformation from the reference space to physical space. To implement these refractive indexes, the dielectric constant is used

$$n(x,y) = \sqrt{\epsilon_r(x,y)} \quad (2)$$

This result allows the implementation of the conformal transformation with fully dielectric metamaterials. Unfortunately, the relative dielectric constant results in an impedance mismatch which adds internal reflections inside the domain. Therefore, minimizing the dielectric constants is crucial to maintain the proper operation of the CTO.

Another inherent problem of the CTO, is that the resulting dielectric constants may fall below unity. Hence, implementing CTO with purely dielectric material can't be achieved with these dielectric constants. To resolve this issue, optical path rescaling [1] can be used. This is done by defining a rescaling function where the gradient only changes normal to the phase front of propagating wave. With this constraint, the propagation direction of the Electro-Magnetic wave is unchanged. Thus, it is possible to rescale the dielectric constants without changing the propagation inside the device.

Moreover, the absolute phase for automotive RADAR antennas can be arbitrary. Thus, the optical path length does not have to be constrained, in contrast to the original proposed rescaling method. This relaxation of the rescaling method gives us larger freedom to reduce the dielectric constants of the device. This also helps to mitigate the internal reflection due to impedance mismatch.

4.2 Numerical results from the conformal transformation optics

As mentioned above, one of the challenges in designing wide FoV antennas are the surface waves on the ground plane. These surface waves diffract from different spatial inhomogeneities they encounter such as the edge of the ground plane. The diffracted waves superimpose creating a ripple on the radiation pattern. Figure 1 shows an example of this problem. In this example the structure is $1.9\lambda_0$ where λ_0 is the free space wavelength. The radiating element itself is a slot antenna with a width of $\frac{\lambda_0}{100}$ which radiates isotropically, and hence it is omnidirectional in the azimuth plane. This size is chosen since it is in the same order of magnitude as the element size of the automotive radar. This example specifically demonstrates the issue in terms of the appearance of the ripple in the RADAR antenna radiation pattern.

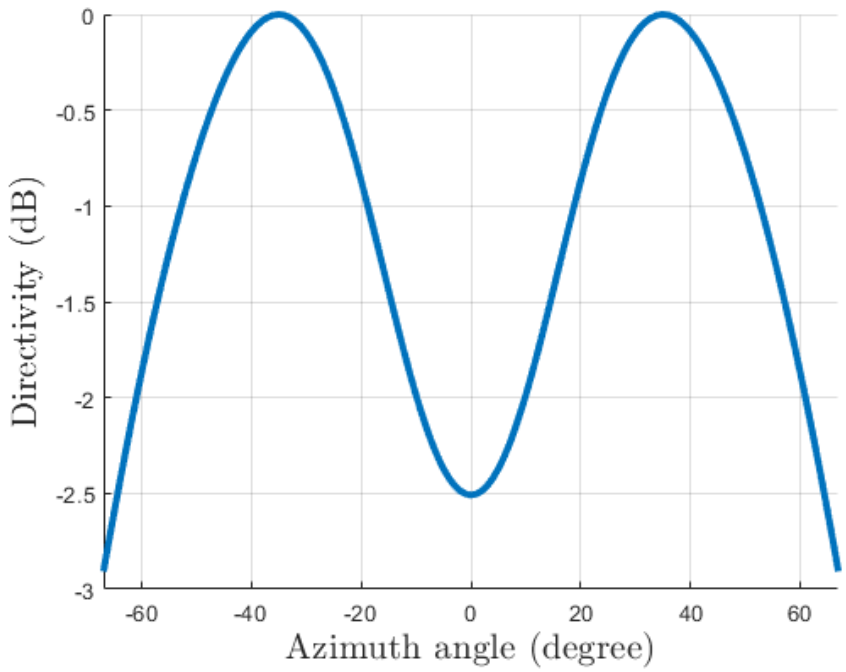

Figure 1. Normalized radiation pattern for an isotropic radiator on a finite ground plane.

A solution to this problem is proposed by optimizing the shape of the ground plane in order to minimize the ripple on the radiation pattern. Figure 2 shows the optimized ground plane for the minimization of the ripple. To demonstrate the effectiveness of the proposed rescaling from section 4.1, a number of optimizations have been done with different values of Δy_{max} which is the scaling factor of the optimized ground plane shown in Figure 2. Figure 3 shows the resulting ripple as a result of the optimization for different values of Δy_{max}. Furthermore, Figure 4(a) shows the impact of internal reflection due to the dielectric implementation without rescaling and Figure 4(b) shows the purely dielectric implementation with rescaling.

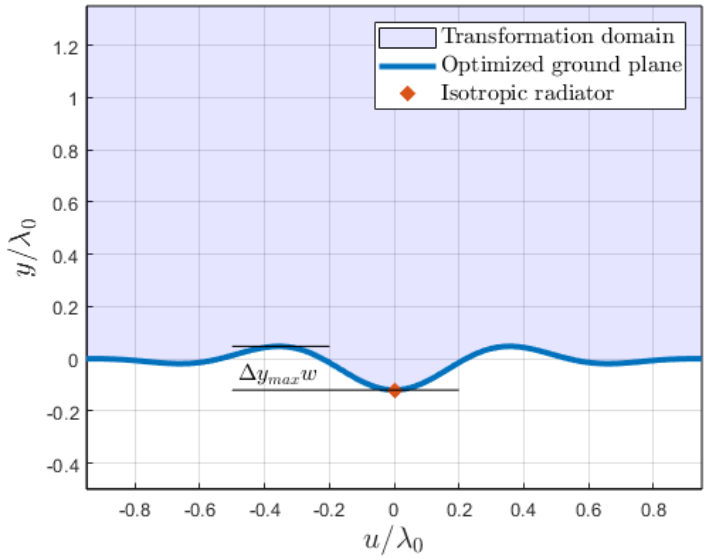

Figure 2. Optimized ground plane to minimize the radiation pattern ripple

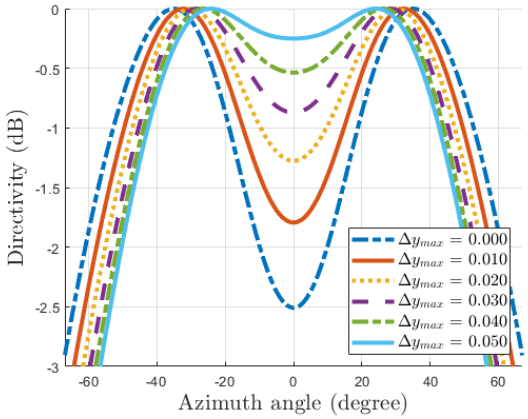

Figure 3. Normalized radiation patterns of the optimized ground plane for different limits of the ground plane curve

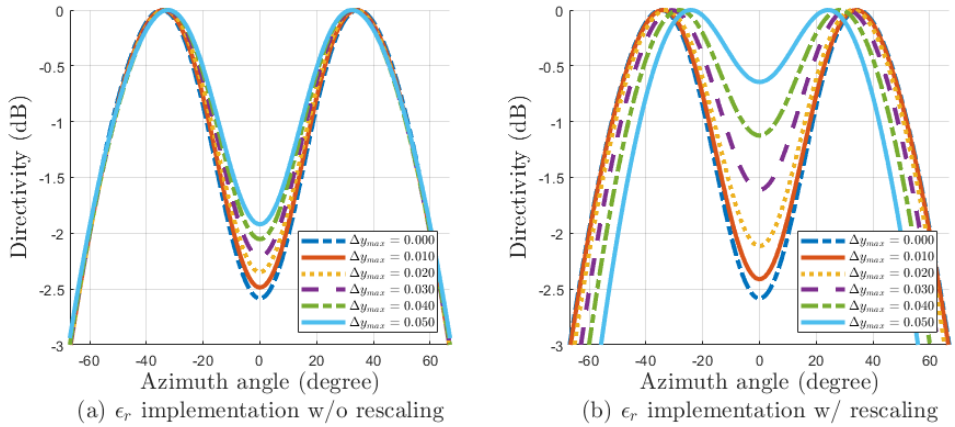

Figure 4. Normalized radiation patterns of the dielectric implementations of the CTO optimized ground plane.

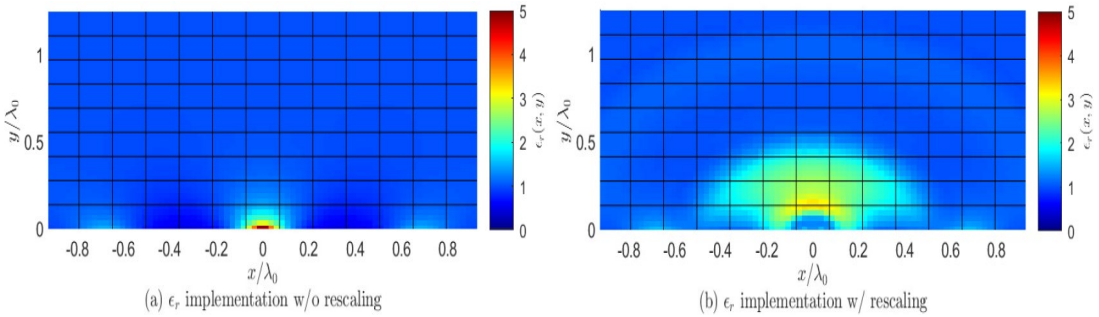

Figure 5. Permittivity distribution from the conformal transformation for the maximum curvature with $\Delta y_{max} = 0.050$.

As can be seen from Figure 4, the ripple can be greatly reduced by introducing a deformed ground plane. The rescaling method allows for the implementation of this deformed ground plane employing a CTO with purely dielectric materials. Furthermore, the reduction of the dielectric constants also minimizes the error induced by the internal impedance mismatch. Figure 5 shows the dielectric constants for the optimisation with $\Delta y_{max} = 0.05$.

4.2.1 Simulation results of CTO improved slotted Gap waveguide antenna

The CTO works in a 2D scenario as shown above. Moreover, when extruding this solution out of the 2D-plane, a 3D structure can be built with the same conformal transformation. Using this, CTO can be used to realize physical devices. The ripple for a slotted GW antenna has been minimized using a similar approach as for the isotropic radiator in the 2D approach presented above.

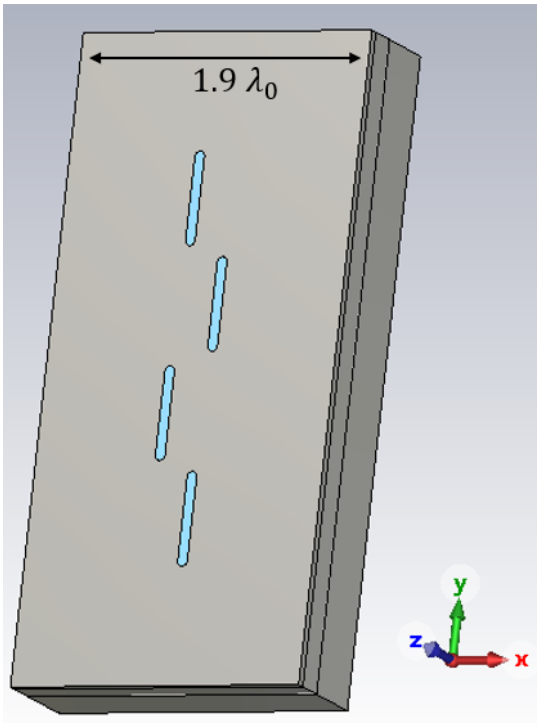

Figure 6. Reference slotted GW antenna.

Figure 6. The reference GW antenna is shown. A design with 4 slots has been chosen, and impedance matched to the feeding port below -15 dB S11 from 76 to 81 GHz. The upper layer of the structure, or slot layer, has been chosen with a width of $1.9\lambda_0$ to demonstrate the issue arising from surface waves on the antenna body.

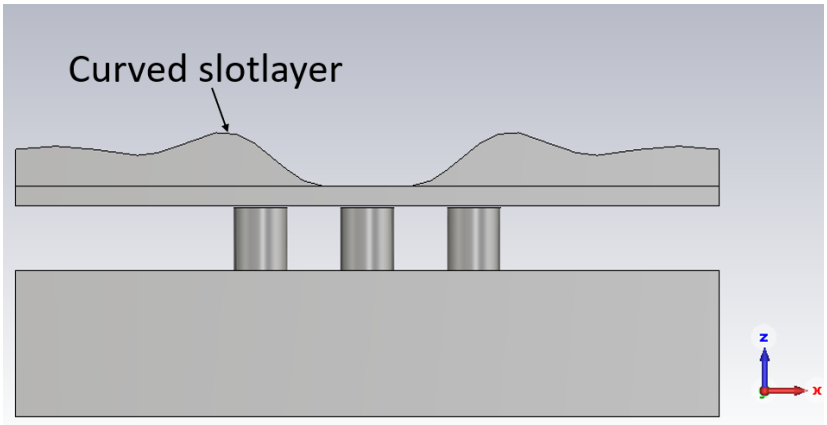

Figure 7. Optimization result of the curved slot layer to minimize the radiation pattern ripple

As the optimization presented above for the 2D case, a curved surface has been used to optimize the slot layer and minimize the ripple on the radiation pattern. This optimization result is shown in Figure 7. After computing the CTO and applying the rescaling function a 3D profile for the dielectric constants can be generated. To create the resulting dielectric constant in a physical structure, a unit cell has been used similarly to [2], where the effective dielectric constant is determined by the weighted sum of the dielectric material inside the unit cell. The Unit cell which has been used is shown in Figure 8. In this unit cell, the effective dielectric constant

$$\epsilon_{eff} = \frac{(P_y - w)}{P_y}\epsilon_1 + \frac{w}{P_y}\epsilon_2, \quad (3)$$

where ϵ_1 and ϵ_2 are the dielectric constants of vacuum and the material in the unit cell. Typically, the implementation of such unit cell should be on the scale of $\frac{\lambda}{10}$ or even smaller. However, the propagation is quasi- constant in the out-of-plane direction of the conformal transformation (y-direction in Figure 8), resulting in a unit cell that can be enlarged to approximately $\frac{\lambda}{4}$ because of this. The resulting structure has been shown in Figure 9 where a material was chosen with the same dielectric constant as the maximum dielectric constant of the CTO after rescaling with a value of 3.5.

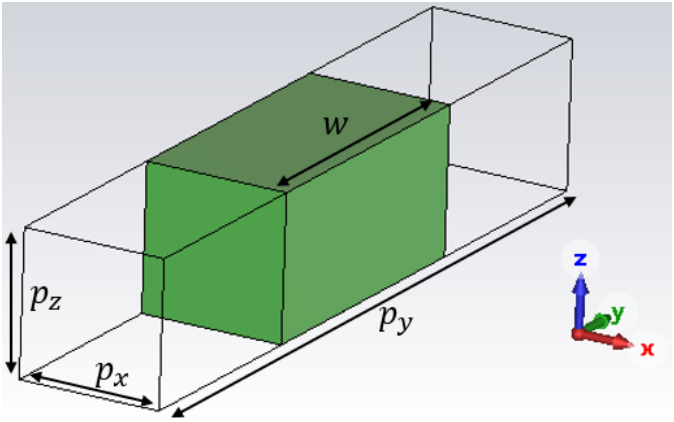

Figure 8. Unit cell for the physical CTO implementation.

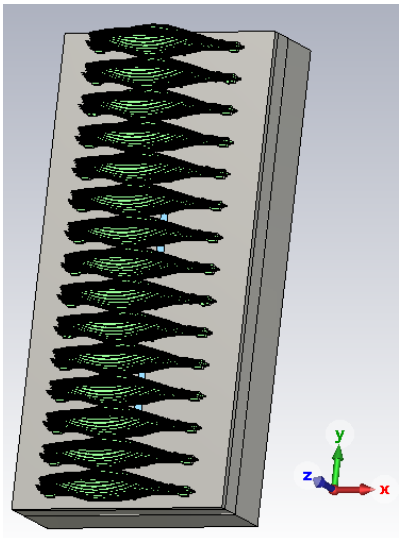

Figure 9. Slotted GW antenna with dielectric implementation of the CTO slot layer.

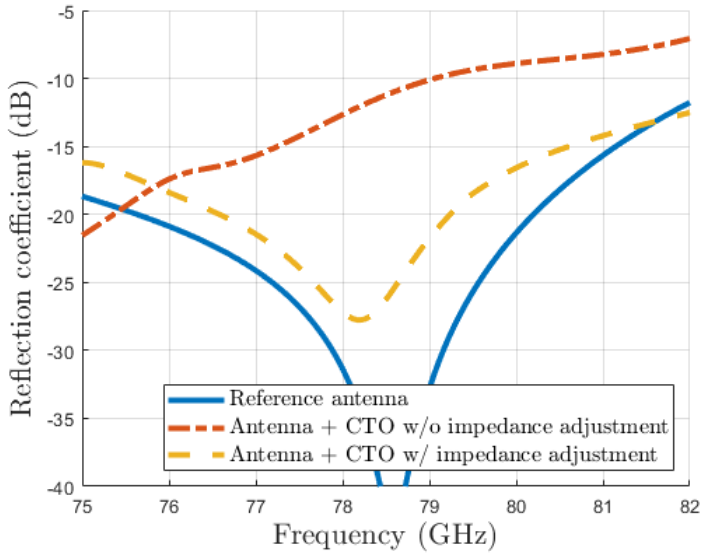

Figure 10. Reflection coefficient of the slotted GW antenna.

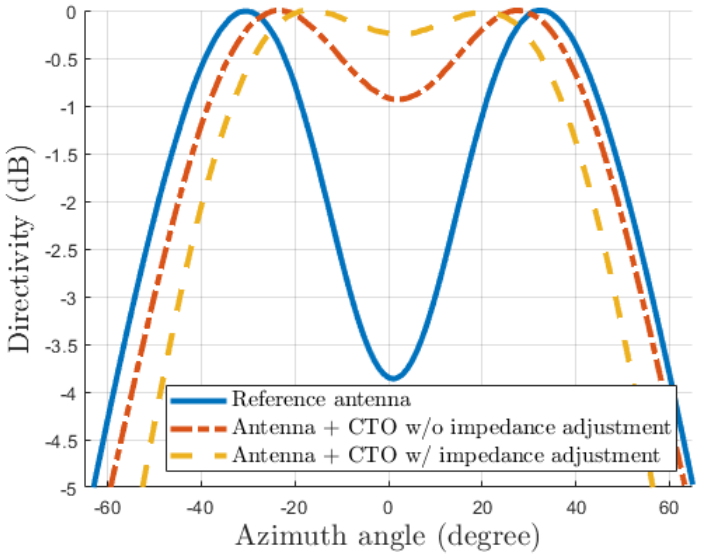

Figure 11. Normalized radiation pattern for the slotted GW antenna.

Since the impedance of the dielectric structure is inherently different from the free space impedance, the antenna experiences a loading effect mainly affecting the reflection coefficient of the antenna. To mitigate this, the antenna element is slightly adjusted to compensate this effect. This is done by increasing the offset of the slots from the centre of the antenna. The corresponding reflection coefficients are shown in Figure 10. Finally, the resulting radiation pattern for the whole structure in Figure 11. It is demonstrated that a considerable reduction of the ripple from the slotted waveguide using CTO can be obtained.

5 Modelling techniques for multipurpose phased array antennas at mm-Wave

This section describes the design process and simulation results of a 1 × 10 linear Franklin sub-array antenna and two adjacent 5 × 10 linear arrays comprising each 5 elements that has been performed by ESR 1. Both arrays have been jointly designed on the same PCB. The designed array antennas are simulated and optimized with the CST Microwave Studio simulation software. They are used here for purpose of illustrating the correlation and nonorthogonality of beamforming fields.

5.1 Design of Franklin Array Antennas

The configuration of a 1×10 series-fed modified microstrip Franklin array antenna is shown in Figure 12. This microstrip linear Franklin array with 10 rectangular elements is designed to operate at 77 GHz and designed on the Rogers RT5880 substrate with a thickness of 0.252 mm, ϵr = 2.2 and tanσ = 0.0009. The dimensions of the elements are given in Table 1. An inset microstrip feed line at the input of the subarray is used as the excitation for the whole linear sub-array. Symmetric open circuit stubs are used to achieve impedance matching. Figure 13 shows the return loss results demonstrating a good impedance matching at the input of antenna and between elements. Also, the simulated realized gain at azimuth angle (φ = 0°) values for the 76 to 78 GHz frequency band are shown in Figure 13. The Chebyshev tapering technique is applied to change the widths of each of the rectangular microstrip patches according to the Chebyshev coefficients values. The reduced side lobe level at 13.6 dB from the main beam gain is obtained at the operating frequency of 77 GHz. The simulated E-plane (φ = 0°) and H-plane (φ = 90°) radiation patterns are shown in Figure 14.

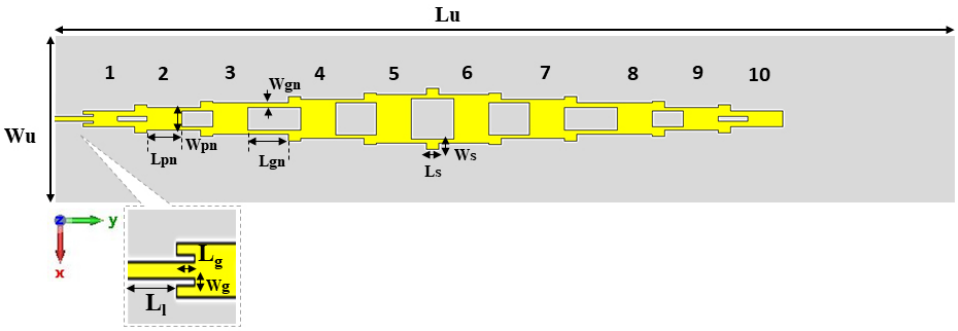

Figure 12. The 1 × 10 Chebyshev tapered rectangular Franklin array antenna configuration and corresponding element numbers.

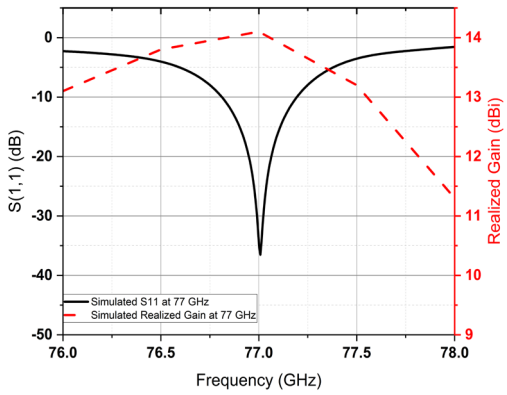

Figure 13. Simulated Reflection coefficient and realized gain for the Franklin sub-array at 77 GHz.

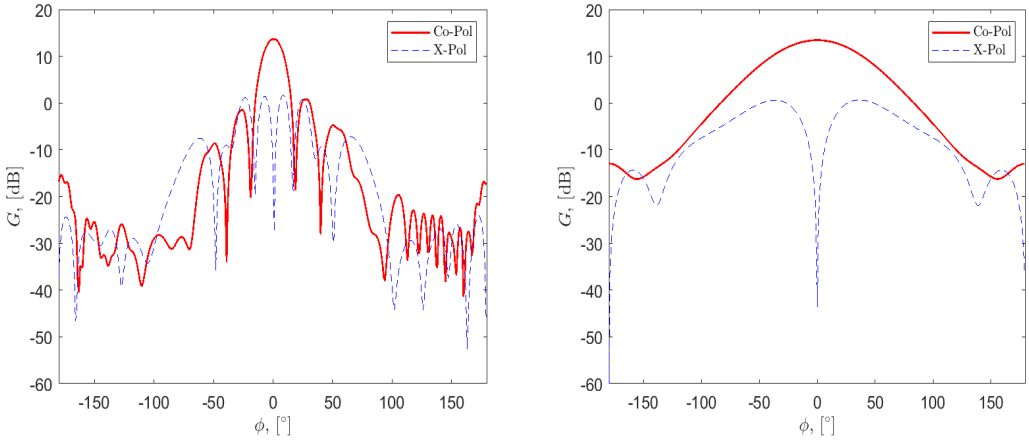

(a) (b)

Figure 14. Co-polarized and X-polarized simulated patterns of the 1×10 Franklin sub-array at 77 GHz (a) E-plane and (b) H-plane.

Table 1. Antenna Design Measures.

AEL (n)	1&10	2&9	3&8	4&7	5&6
L_{pn}(mm)	1.12	1.12	1.12	1.12	1.12
W_{pn}(mm)	0.508	0.724	1	1.24	1.54
L_{gn}(mm)	0.935	0.982	1.67	1.28	1.34
W_{gn}(mm)	0.18	0.11	0.142	0.11	0.12
L_s(mm)	0.398	0.398	0.398	0.398	0.398
W_s(mm)	0.2	0.2	0.2	0.2	0.2
Parameter	L_u	W_u	L_l	L_g	W_g
Value(mm)	29.4	5.5	0.924	0.34	0.1

Two 5 × 10 array antennas located side by side are simulated. They may represent an example of arrays that can be used for either communication or sensing, or either as the transmitter (Tx) and receiver (Rx) parts of a communication system or as the Tx and Rx parts of a radar system. The two adjacent arrays are shown in Figure 15. Beamforming is computed for each array and

the radiation patterns are scanned from φ = −25° to φ = 25° in the azimuth plane as shown in Figure 16.

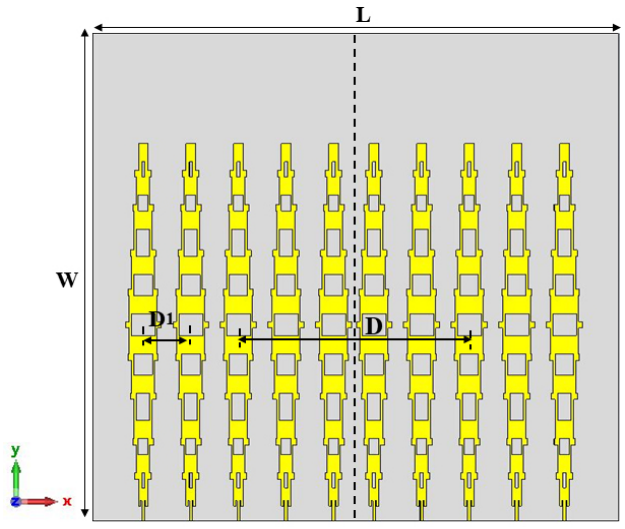

Figure 15. Geometry of the simulated 5 × 10 array antenna based on Franklin sub-arrays.

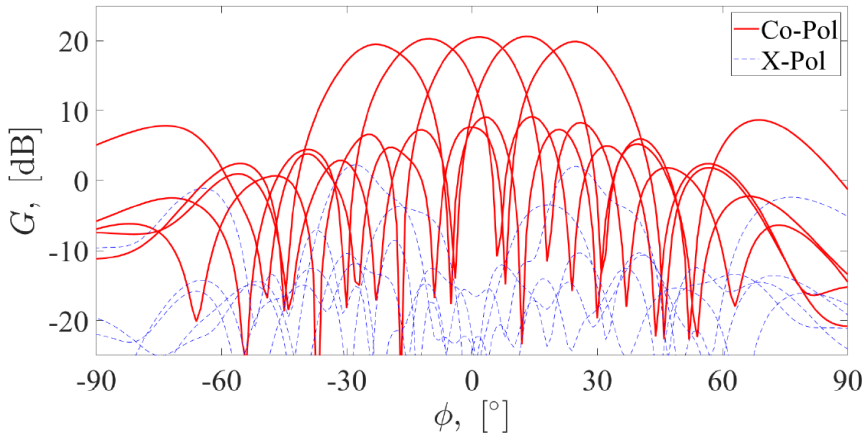

Figure 16. Co-polarized and X-polarized simulated scanned patterns (E-plane) at 77 GHz of the 5 × 10 array antenna.

5.2 Correlation and the Non-Orthogonality of Beamforming Patterns

One of the major problems in joint communication and sensing systems is the coupling of transmitting (TX) antenna and receiving (RX) antenna signal paths as well as the potential interference between radar and communication radiation patterns of the antennas. The performance of different linear patch antenna array architectures in terms of self-interference cancellation performance and obtained maximum gain in the beam steering range [3]. The proposed arrays are designed to operate with the implementation of a self-interference cancellation algorithm required for true in-band full-duplex JCAS operation at the same frequency band. The correlation and non-orthogonality of radiation patterns has been vastly studied, see e.g. [4], [5].

5.2.1 Correlation of Beamforming Fields

An array antenna usually produces beams at different scanning directions. We introduce the beam correlation (BC) of an array antenna

$$\rho_{11,\mathrm{BC}}(\alpha,\beta)=\frac{|\oint F_1(\alpha)\cdot F_1^*(\beta)\mathrm{d}\Omega|^2}{\oint|F_1(\alpha)|^2 d\Omega \oint|F_1(\beta)|^2 d\Omega}, \quad (4)$$

where here $F_1(\alpha)$ is the beamforming field of an array antenna at scanning (beamforming) angle α and $F_1(\beta)$ is the beamforming field of the same array antenna at scanning angle β.

Clearly, beams sufficiently separated in the angular domain can result in a low correlation, while obviously the correlation is full, i.e., $\rho_{11,\mathrm{BC}}(\alpha, \beta) = 1$ for $\alpha = \beta$. Similarly, we can define the same type of correlation for two co-located or two distributed array antennas as a function of the scanning angles of their beams

$$\rho_{12,\mathrm{BC}}(\alpha,\beta)=\frac{|\oint F_1(\alpha)\cdot F_2^*(\beta)\mathrm{d}\Omega|^2}{\oint|F_1(\alpha)|^2 d\Omega \oint|F_2(\beta)|^2 d\Omega}, \quad (5)$$

where $F_1(\alpha)$ and $F_2(\beta)$ are the far-fields corresponding to two beamforming array antennas scanned in directions α and β. We can interpret (4) as the beamforming- directional auto-correlation, while (5) is the beamforming field directional cross-correlation. Thus, the beam forming field directional auto-correlation for array antenna 2 will be denoted by $\rho_{11,\mathrm{BC}}$. It is straightforward to see that (5) becomes exactly zero if the beams of the two antennas are orthogonal in polarization, but as above for the single antennas, the correlation can be reduced if the arrays are separated in space or the produced beams are sufficiently separated in directions. Depending on the application, you might require that the two arrays generate highly correlated beams while scanning in the same direction, i.e., $\rho_{12,\mathrm{BC}}(\alpha, \beta) = 1$ when $\alpha = \beta$ and 0 in all other directions. The condition applies in this case for each of the array antennas Ie, i.e., $\rho_{11,\mathrm{BC}}(\alpha, \beta) = \rho_{22,\mathrm{BC}}(\alpha, \beta) = 1$ and 0 in all other directions. In this case, a useful measure of the overall correlation between the two antennas can be characterized by the product:

$$\rho_{12,\mathrm{BCW}}(\alpha,\beta)=\sqrt{\rho_{12,\mathrm{BC}}\sqrt{\rho_{11,\mathrm{BC}}\rho_{22,\mathrm{BC}}}} \quad (6)$$

where $\rho_{12,\mathrm{BC}}$, $\rho_{11,\mathrm{BC}}$ and $\rho_{22,\mathrm{BC}}$ are given by the equations above and all depend on α and β, which have been omitted for compactness. When the two array antennas have identical performance then $\rho_{12,\mathrm{BCW}} = \rho_{11,\mathrm{BC}} = \rho_{22,\mathrm{BC}}$. The advantage of (6) is that it condenses the correlation between the beams of the two array antennas and the beams of the individual array antennas into one parameter.

Figure 17 shows the beam correlation between the 5 beams shown in Figure 16 as a function of the scanning angles of the two simulated arrays. The subplots show (a) $\rho_{12,\mathrm{BCW}}$, (b) $\rho_{11,\mathrm{BCW}}$, (c) $\rho_{22,\mathrm{BC}}$, and (d) $\rho_{12,\mathrm{BCW}}$. As can be seen from Figure 17(a) the two arrays produce beams that are fully uncorrelated for all the considered scanning angles. This means that in a RIMP channel the beams of the two adjacent channels are fully uncorrelated even if they point in the same direction. On the other hand, the beams from the same array are correlated mainly when pointing in the same directions, i.e., it is the same beam. However, as the beams are pointing in different directions the correlation rapidly decreases. The compound figure of merit shown in Figure 17(d) the correlation will be stay low independently of the correlation of the individual array antennas. Hence, in this specific case the behavior of each individual array does not have

a major impact on the beam correlation. Figure 18 just reinforces the observations from above. Both arrays produce uncorrelated beams. And as expected beams from the same array become highly correlated (auto-correlated) when looking at close points in the angle domain, in the other directions correlation drops after 5° or 10°, see Figures 18(b) and (c). The compound effect shown in Figure 18(d) is dominated by beamforming de-correlation between the two spatially separated array antennas.

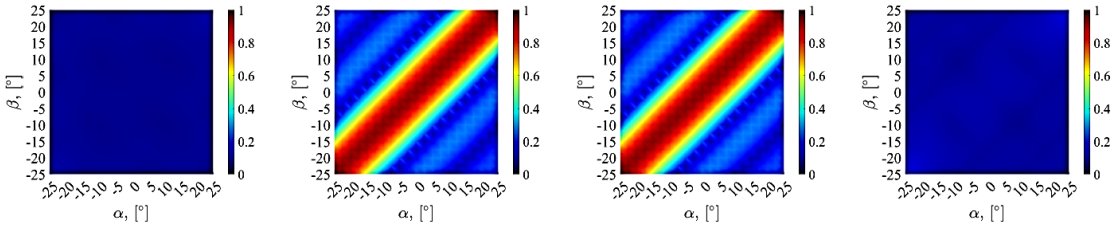

Figure 17. Beam correlation between the 5 beams shown in Figure 16 as a function of the scanning angles of the two simulated arrays. (a) ρ12,BC, (b) ρ11,BC, (c) ρ22,BC, and (d) ρ12,BCW.

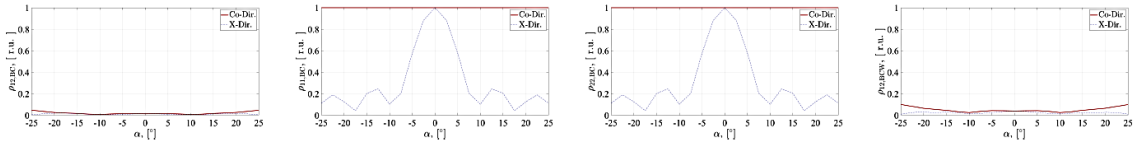

Figure 18. Beam correlation between the 5 beams shown in Figure 16 as a function of the scanning angle. Two cuts are taken from Figure 17, along the diagonal denoted by Co-Dir., and along the anti-diagonal denoted by X-Dir. (a) ρ12,BC, (b) ρ11,BC, (c) ρ22,BC, and (d) ρ12,BCW.

5.2.2 Non-Orthogonality of Beamforming Fields

Following a similar line of thought as above we here introduce the beam non-orthogonality (BNO) of an array antenna:

$$\rho_{11,\mathrm{BNO}}(\alpha,\beta) = \frac{|F_1(\alpha)\cdot F_1^*(\beta)|}{|F_1(\alpha)||F_1(\beta)|} \qquad (7)$$

where here $F_1(\alpha)$ is the beamforming field of an array antenna at scanning (beamforming) angle α and $F_1(\beta)$ is the beamforming field of the same array antenna at scanning angle β as defined above. Also, here we can introduce the beam non-orthogonality for two co-located or two distributed array antennas as a function of the scanning angles of their beams:

$$\rho_{12,\mathrm{BNO}}(\alpha,\beta) = \frac{|F_1(\alpha)\cdot \boldsymbol{F_2^*}(\beta)|}{|F_1(\alpha)||\boldsymbol{F_2}(\beta)|} \qquad (8)$$

where, as above, $F_1(\alpha)$ and $F_2(\beta)$ are the far-fields corresponding to two beamforming array antennas scanned in directions α and β. Hence, a condensed parameter follows from the above definitions:

$$\rho_{12,\mathrm{BNOW}}(\alpha,\beta) = \sqrt{\rho_{12,\mathrm{BNO}}\sqrt{\rho_{11,\mathrm{BNO}}\rho_{22,\mathrm{BNO}}}} \qquad (9)$$

where $\rho_{12,\mathrm{BNO}}$, $\rho_{11,\mathrm{BNO}}$ and $\rho_{22,\mathrm{BNO}}$ have been defined above and all depend on α and β, which have been omitted for compactness. Following a symmetric analysis as above, we can clearly see that when both array antennas have identical performance then $\rho_{12,\mathrm{BNO}} = \rho_{11,\mathrm{BNO}} = \rho_{22,\mathrm{BNO}}$. The advantage of (9), as in the case of (6), relies on the fact that it condenses the non-orthogonality

between the beams of the two arrays antennas and the beams of the individual array antennas into one parameter.

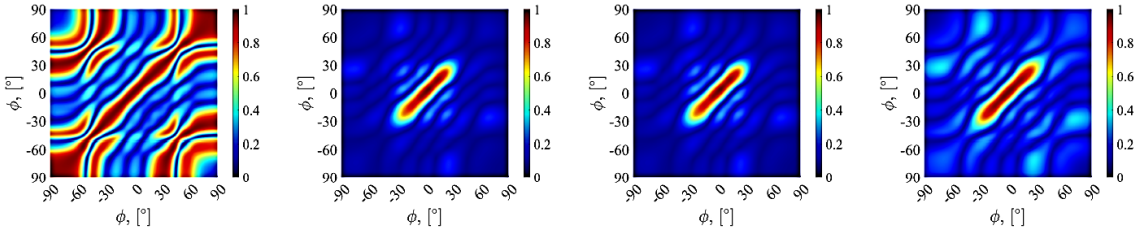

Figure 19. Beam non-orthogonality for the 5 beams shown in Figure 16 as a function of azimuth. All five beams are shown simultaneously. (a) ρ12,BNO, (b) ρ11,BNO, (c) ρ22,BNO, and (d) ρ12,BNOW.

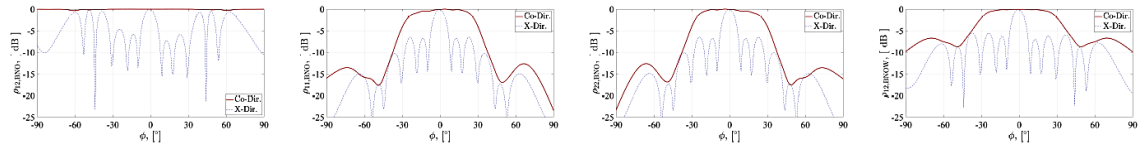

Figure 20. Beam non-orthogonality for the 5 beams shown in Figure 16 as a function of azimuth. All five beams are shown simultaneously. Two cuts are taken from Figure 19, along the diagonal denoted by Co-Dir. and along the anti-diagonal denoted by X-Dir. (a) ρ12,BNO, (b) ρ11,BNO, (c) ρ22,BNO, and (d) ρ12,BNOW.

Figure 19 shows the beam non-orthogonality for the 5 beams shown in Figure 16 as a function of azimuth angle. All five beams are shown simultaneously. The specific subplots show (a) $\rho_{12,\mathrm{BNO}}$, (b) $\rho_{11,\mathrm{BNO}}$, (c) $\rho_{22,\mathrm{BNO}}$, and (d) $\rho_{22,\mathrm{BNOW}}$. As can be seen from Figure 19(a) there is a high beam correlation at different direction, but mostly in the direction where both arrays' beams are pointing in the same direction. Figure 19(b) and (c) show that the beam non-orthogonality of both array antennas is confined to the main plane of radiation and within the FoV of the scanned beams (compare to Figure 16). The compound figure of merit shown in Figure 19(d) illustrates that even if the non-orthogonality is high in many direction of observation, the relevance is weighted by the behavior of each individual array due to the limited FoV. Figure 20 is the beam non-orthogonality for the 5 beams shown in Figure 16 as a function of azimuth. Two cuts are taken from Figure 19, along the diagonal denoted by Co-Dir. and along the anti-diagonal denoted by X-Dir. All five beams are shown simultaneously. (a) $\rho_{12,\mathrm{BNO}}$, (b) $\rho_{11,\mathrm{BNO}}$, (c) $\rho_{22,\mathrm{BNO}}$, and (d) $\rho_{12,\mathrm{BNOW}}$. These plots are presented to further clarify the non-orthogonality of the beams of the two array antennas when they are pointing towards the same direction (Co-Dir.) and where they are pointing away from each other (X-Dir.). Clearly, as explained above the two arrays are non-orthogonal in the main direction of radiation of the beams.

6 Conclusion

This report has discussed numerical modelling techniques have for joint communication and sensing as well as for automotive RADAR. For automotive RADAR, GW technology has been chosen as the main focus because of the associated electrical performance as well as its robustness for large scale manufacturing. To mitigate the negative electrical effects from the integration of the antenna with the radome, ESR 3 has proposed to use conformal transformation optics as well as optical path rescaling to enhance the performance of the RADAR phased array antennas. A proof of concept has been shown in simulation where conformal transformation optics successfully minimizes the ripple on the radiation pattern.

For Joint communication and sensing, a mayor concern is the isolation between both parts of the system. To investigate the isolation of two arrays in such a system, various figure of merit are introduced which address the orthogonality between the beams generated by two adjacently located phased array antenna. We illustrate the significance of the proposed figures of merit for evaluation of a joint communication and sensing system on an antenna model of two sub-arrays designed on the PCB technology. It has been shown that the propagation channel has a high impact on the beam orthogonality, or rather beam non-orthogonality. Hence, this aspect needs to be considered when designing adjacently located phased array antennas for joint communication and sensing systems at mmWave frequencies.

The work presented here show results towards the development of low cost, low form-factor and highly efficient phased array MIMO antenna and RADAR antenna prototypes and layouts embedded on the bodywork of a car for V2X/cellular applications. And also towards the development of an all-inclusive characterization of the joint communication and sensing antennas at component and system levels, which are fundamental objectives of WP1.

References

[1] Hossein Eskandari and Tomas Tyc. “Controlling refractive index of transformation-optics devices via optical path rescaling”. In: Scientific Reports 9 (Dec. 2019). DOI: 10.1038/s41598-019-54516-0.

[2] Juan Lei et al. “Experimental demonstration of conformal phased array antenna via transformation optics”. In: Scientific Reports 8.1 (Feb. 2018), p. 3807. ISSN: 2045-2322. DOI: 10.1038/s41598-018-22165- 4. URL: https://doi.org/10.1038/s41598-018-22165-4.

[3] M. Heino, C. Baquero Barneto, T. Riihonen and M. Valkama,” Design of Phased Array Architectures for Full-Duplex Joint Communications and Sensing,” 2021 15th European Conference on Antennas and Propagation (EuCAP), 2021, pp. 1-5, doi: 10.23919/EuCAP51087.2021.9411430.

[4] R. G. Vaughan and J. B. Andersen,” Antenna diversity in mobile communications,” in IEEE Transactions on Vehicular Technology, vol. 36, no. 4, pp. 149-172, Nov. 1987, doi: 10.1109/T-VT.1987.24115.

[5] G. F. Pedersen, S. Widell and T. Ostervall, ”Handheld antenna diversity evaluation in a DCS-1800 small cell,” Proceedings of 8th International Symposium on Personal, Indoor and Mobile Radio Communications - PIMRC ’97, 1997, pp. 584-588 vol.2, doi: 10.1109/PIMRC.1997.631099.